EUROPEAN FUSION DEVELOPMENT AGREEMENT

EFDA-JET-PR(04)60

M.E. Fenstermacher, T.H. Osborne, A.W. Leonard, P.B. Snyder,
D.M. Thomas, J.A. Boedo, T.A. Casper, R.J. Groebner, M. Groth,
M.A.H. Kempenaars, A. Loarte, G.R. McKee, W.M. Meyer, G. Saibene,
M.A. VanZeeland, X.Q. Xu, L. Zeng, DIII-D Team and JET EFDA Contributors*

Structure, Stability and ELM Dynamics of the H-Mode Pedestal in DIII-D

Structure, Stability and ELM Dynamics of the H-Mode Pedestal in DIII-D

M.E. Fenstermacher,[2] T.H. Osborne,[1] A.W. Leonard,[1] P.B. Snyder,[1]
D.M. Thomas,[1] J.A. Boedo,[1] T.A. Casper,[3] R.J. Groebner,[2] M. Groth,[1]
M.A.H. Kempenaars,[2] A. Loarte,[4] G.R. McKee,[5] W.M. Meyer,[6] G. Saibene,[2]
M.A. VanZeeland,[4] X.Q. Xu,[1] L. Zeng,[4] DIIIÐ Team [7] and JET EFDA Contributors*

[1]General Atomics, San Diego, California, United States of America
[2]Lawrence Livermore National Laboratory, Livermore, California, USA
[3]University of California, San Diego, California, USA
[4]FOM-Rijnhuizen, Assoc. Euratom-FOM, TEC, Nieuwegein, Netherlands
[5]EFDA-CSU, Max-Planck-Institut for Plasmaphysik, Garching, Germany
[6]University of Wisconsin, Madison, Wisconsin, USA
[7]University of California Los Angeles, Los Angeles, California, USA
** See annex of J. Pamela et al, "Overview of Recent JET Results and Future Perspectives", Fusion Energy 2002 (Proc.19 th IAEA Fusion Energy Conference, Lyon (2002)).*

Preprint of Paper to be submitted for publication in
Nuclear Fusion

ABSTRACT

Experiments are described that have increased understanding of the transport and stability physics that set the H–mode edge pedestal width and height, determine the onset of Type-I edge localized modes (ELMs), and produce the nonlinear dynamics of the ELM perturbation in the pedestal and scrape-off layer (SOL). Models now exist for the n_e pedestal profile and the pe height at the onset of Type-I ELMs, and progress has been made toward models of the T_e pedestal width and nonlinear ELM evolution. Similarity experiments between DIII–D and JET suggested that neutral penetration physics plays an important role in the relationship between the width and height of the–n_e pedestal. Plasma physics appears to dominate in setting the T_e pedestal width. Measured pedestal conditions including edge current at ELM onset agree with intermediate-n peeling-ballooning (P-B) stability predictions. Midplane ELM dynamics data show the predicted (P-B) structure at ELM onset, large rapid variations of the SOL parameters, and fast radial propagation in later phases, similar to features in nonlinear ELM simulations.

I. INTRODUCTION

This paper describes experiments that were focused on optimizing pedestal parameter measurements to determine the transport and stability physics that set the H–mode edge pedestal width and height, the onset conditions for Type-I edge localized mode (ELM) instabilities, and the nonlinear dynamics of the ELM perturbation observed in the pedestal and midplane scrapeoff layer (SOL). These are critical issues for future burning plasma devices such as ITER [1] because for stiff profiles the height of the pedestal determines the overall confinement [2], and the size of the ELMs determines divertor target lifetimes [3]. The experiments were carried out primarily on DIII–D with additional results coming from dimensionally similar plasmas in DIII–D and JET.

Results are in agreement with models for the density pedestal width and the pressure gradient at the onset of Type-I ELMs, and show that progress has been made toward generating models of the temperature pedestal width (transport barrier) and nonlinear ELM evolution. Previous studies of pedestal structure have been done for many individual devices including MAST [4], C–Mod [5], ASDEX Upgrade (AUG) [6,7], JET [8] and DIII–D [9]. Recently pedestal structure has been examined through similarity studies between C–Mod/DIII–D [10] and between JET/JT–60U [11]. Studies of Type-I ELM evolution have also been reported from AUG [12–14], JET [15,16] and JT–60U [17,18] while studies of Type-III ELM evolution have been done at MAST [19,20] and TCV [21]. The new measurements reported in this paper show that the density pedestal width is consistent with neutral penetration physics playing a significant role in setting the density pedestal parameters. The pressure pedestal gradient is limited by the stability of coupled peeling-ballooning (P-B) instabilities at the edge. In similarity experiments with fixed pedestal beta, β, collisionality, ν^*, normalized gyroradius, ρ^* and safety factor, q, the transport barrier width, Δ_T, scaled with minor radius, a. When ρ^* was varied at fixed (β, ν^*, q), Δ_T/a was nearly independent of ρ^*, and ELM size decreased as ρ^* decreased in agreement with changes in the radial mode width of the most unstable P-B mode. New edge current measurements confirmed the edge bootstrap current models used in

the edge stability calculations. Finally, new fast data and initial nonlinear ELM simulations indicated that ELMs have a complicated spatial and temporal structure in the pedestal and SOL. Some initial scaling of these results to future devices is possible, as described below.

The paper is organized as follows. The experimental techniques and some of the important diagnostic measurements are described in Sec.2. Experimental results are described in Sec.3 including those from the pedestal similarity experiments, the edge stability characterization, and the nonlinear ELM dynamics. A summary and conclusions are given in Sec.4.

2. EXPERIMENTAL TECHNIQUES AND DIAGNOSTICS

The pedestal transport and stability mechanisms were investigated both with new diagnostics in DIII–D and in similarity experiments with matched plasma shape and dimensionless pedestal parameters between DIII–D and JET. The similarity experiments focused on determining the physics mechanisms that set the pedestal widths. These were done in matched Lower Single-Null (LSN) discharges with optimized shapes for pedestal profile diagnostics on JET (the so-called DOC-L shape with elongation $\kappa = 1.72$ and average triangularity, $\delta_{avg} = 0.27$ and the DOC-U shape with $\kappa = 1.68$ and $\delta_{avg} = 0.35$) [22,23]. For JET, typical discharge parameters were plasma current I_p = 1.2–2.5MA, major radius R = 2.95m, minor radius a = 0.93m, and heating power in the range P_{inj} = 4.9–17.0MW. For the pedestal similarity experiments, the dimensionless parameters $\beta \sim nT/B_T^2$, effective collisionality, $\nu^* \sim nqRA^{3/2}/T^2$, effective Larmor radius, $\rho^* \sim T^{1/2}/a\ B_T$ and safety factor, $q \sim a^2 B_T/RI_p$ were matched at the top of the pedestal, although they could not be matched across the entire transport barrier profile. Here B_T is the toroidal field, q is the safety factor at 95% flux, n and T are the density and temperature respectively, and A is the aspect ratio, R/a. In pulses with matched shape, maintaining fixed β, ρ^*, ν^*, and q at the top of the pedestal requires that density, temperature, toroidal field, and plasma current scale as $n^{ped} \sim a^{-2}$, $T^{ped} \sim A^{5/4}\ a^{-1/2}$, $B_T \sim A^{5/8}\ a^{-5/4}$, and $I_p \sim A^{-3/8}\ a^{-1/4}$ respectively. Studies of ρ^* dependence were done by varying B_T. In this case with fixed q, maintaining fixed β and ν^* at the top of the pedestal requires that $n^{ped} \sim A^{-5/6}\ a^{-1/3}\ B_T^{4/3}$, $T^{ped} \sim A^{5/6}\ a^{1/3}\ B_T^{2/3}$ and $I_p \sim A^{-1}\ a\ B_T$. Toroidal field was varied in JET from B_T = 1.2 to 2.7T.

Parameters in the DIII–D similarity pulses were I_p = 1.18–1.38MA, R = 1.7m, a = 0.6m, $P_{inj} \sim$ 1.12–9.5MW and B_T = 1.0 to 2.1T. Pedestal profiles were measured in JET with an edge LIDAR system (n_e and T_e) and with ECE emission (T_e). On DIII–D, profiles of n_e and T_e were measured with Thomson scattering. The profiles of ion temperature T_i were obtained from charge-exchange recombination (CER) spectroscopy.

Pedestal stability physics studies on DIII–D combined detailed pedestal plasma profile measurements with pedestal current density measurements using a unique new Li-beam polarimetry diagnostic [24] to predict the onset of ELMs from a linear peeling-ballooning theory with all relevant parameters measured. In these studies the plasma shape was optimized for pedestal and near SOL profile measurements with the DIII–D Thomson scattering and CER systems. Small radial excursions of the separatrix were used to further refine the profile measurements. In addition, for the first time the current density in the pedestal region was directly measured [24] simultaneously with the profiles

using polarimetry of an injected lithium beam. Combining magnetics measurements with the measured n_e, T_e, T_i, and edge current density provided all the necessary parameters to generate accurate equilibrium reconstructions and to check theories of bootstrap current generation at the edge and peeling-ballooning stability predictions of ELM onset.

Pedestal dynamics during ELMs were measured on DIII–D with simultaneous fast diagnostics near the outer midplane. These included a tangentially viewing radial array of fast D_α detectors at up to 100kHz [25], a fast reciprocating probe with data acquisition rates of 200kHz for n_e and T_e, and 1MHz for I_{sat} [26], profile reflectometry measurements up to $n_e = 6\text{x}10^{19}$ m^{-3} at 40kHz rate [27], beam emission spectroscopy of radially and poloidally propagating density fluctuations with 1MHz acquisition rate [28], and a very fast interferometer chord viewing radially in from the outer midplane with a 5MHz sampling rate [29].

3. EXPERIMENTAL RESULTS

A. PEDESTAL STRUCTURE

Data from similarity experiments between DIII–D and JET are consistent with neutral penetration physics playing an important role in setting the relationship between the width, Δ_n, and height, n_e^{ped} of the density pedestal. The limited data obtained so far can not however rule out the possibility that ionized particle transport physics also plays an important role in setting the density pedestal as suggested by previous studies [6,13]. For the present comparison, density profiles from low-density pulses in the two devices are overlaid in Fig.1(a) using the scaling for fixed β, ρ^*, ν^*, and q. Although the top of the n_e pedestal in JET could not be determined precisely, the top of the n_e pedestal in DIII–D was clearly further outboard than in JET. In higher density similarity plasmas (Fig.1(c)), the density pedestal width was narrower, scaling as $\Delta_{ne} \sim 1/n_e^{ped}$ in both DIII–D and JET. For both of the density cases, the top of the temperature pedestal (Figs.1(b,d)) was inboard of the density pedestal in DIII–D. The n_e and T_e profiles were nearly aligned in JET for the low-density conditions (Figs.1(a,b)) but the top of the n_e pedestal was outboard of the T_e pedestal at high density (Figs.1(c,d)).

Simulation of these profiles using a neutral penetration model [30–32] reproduced the shape of the profiles including the difference between the two machines in the radial location of the top of the density pedestal (Fig.1(a)) and the narrowing of the density pedestal with increasing density (Fig.1(c)). The neutral penetration model is based on a 1D fluid transport formulation in which the particle diffusion is balanced by neutral ionization in the pedestal and SOL. It takes into account Franck-Condon neutrals and the effect of poloidal variation in the neutral source due to differences in flux expansion around the SOL. Particle diffusivity within the closed flux surfaces is assumed constant and radial convective flux is assumed negligible compared with the diffusive flux. The model is valid in regimes for which T_e, within an ionization mean free path, is in the range of a few tens to a few hundred eV. This condition is typically satisfied for the edge plasmas in the similarity experiments except for the very lowest density cases not considered here. To compute real density profile values from the model requires specification of two free parameters, the flux expansion

weighted by the neutral source, E*, and the diffusivity coefficient on the closed flux surfaces, D_{SOL}. These were obtained by fitting the model to a dataset of density pedestal widths versus pedestal density from a variety of DIII–D pulses. The value of E* is sensitive to the low density, large width part of the dataset from ohmic and L–mode plasmas, while the value of D_{SOL} was determined from higher density H–mode plasmas. Using fixed values of E* = 7 and $D_{SOL} = 0.72 m^2/s$ for both the DIII–D and JET similarity discharges, the predicted profiles matched the measurements (Figs.1(a,c)) at both densities. The model predicts that the width of the density pedestal should scale as the inverse of the density at the top of the pedestal, $\Delta_{ne} \sim 1/n_e^{ped}$, in agreement with the observations. The observed variations in the radial location between the n_e and T_e barriers suggest that physics other than neutral penetration dominates in setting the T_e barrier.

Plasma physics that scales with dimensionless parameters appears to dominate in setting the temperature pedestal width (transport barrier), Δ_T. Some theories suggest that neutral penetration also sets the temperature pedestal width [33]. If this were the case then Δ_T / a would scale as minor radius. However, in these pedestal similarity experiments, Δ_T / a was the same in both machines (Fig.1(b)), suggesting that plasma physics, not neutral penetration controls the transport barrier width. A similar observation was made in DIII–D/C–Mod similarity experiments [34]. Also consistent with this interpretation was that $\Delta_T / a \sim$ constant was true for a range of densities (Figs.1(b,d)).

No obvious variation of Δ_T/a with ρ^* was seen for fixed (β, ν^*, q) at the top of the pedestal during scans of B_T in DIII–D and JET (Fig.2). A factor of 2 variation of ρ^* was obtained in DIII–D by varying B_T from 1.0 to 2.1T and a somewhat smaller variation was obtained in JET. The transport barrier width, time averaged over the ELM cycle, Δ_T/a in Fig.2, shows no clear dependence on ρ^* for the combined dataset from both machines.

B. PEDESTAL STABILITY

Measured ELM onset conditions compared favorably with ELITE intermediate-*n* peelingballooning stability constraints calculated in self-consistent equilibria using the measured pedestal plasma profiles and a model for the edge current density, j^{edge}, that was constrained by new j^{edge} measurements (Fig.3). First direct measurements [35] of the poloidal field in the pedestal (Fig.3(a)), were made at the outer midplane just before ELM onset with a new Li-beam polarimetry diagnostic [36]. The inferred j^{edge} (Fig.3(b)) was consistent with calculations of edge Pfirsch-Schluter and bootstrap currents [37], using the measured pedestal plasma profiles and the NCLASS bootstrap model [38]. Free boundary equilibria that were constrained by the measured j^{edge}, were generated by the equilibrium solver in the CORSICA code [39]. The inverse solver in CORSICA provided an equilibrium solution in (ρ, θ) (i.e. poloidal flux, poloidal angle) with high midplane radial and X-point poloidal resolutions using an optimized, nonuniform grid. Linear stability calculations of ELM onset conditions were done on this equilibrium with the ELITE code [40,41]. In contrast to ELITE calculations for conditions between ELMs that show stability, for these plasma conditions just before ELM onset, ELITE showed instability for the high $n = 30–35$ modes, stability for low $n \leq 15$, and marginal stability for intermediate n modes, $16 \leq n \leq 29$. The mode structure for the most

unstable mode in this case, n = 25 is shown in Fig.4.

The dependence of the normalized ELM energy loss ($\Delta W_{ELM}/W_{ped}$), in the DIII–D ρ* scan from the similarity experiments, was consistent with predicted changes in the peeling-ballooning mode width at the edge, but neutral penetration physics also played a role. As ρ* decreased (Fig.5) the steep gradient region in the measured pressure profile narrowed. The measured plasma profiles before and after ELMs also showed a narrower ELM affected region and reduced ELM energy loss at low ρ*. In addition, the duration of the ELM magnetic fluctuations and their amplitude was smaller at low ρ*. For the narrower pressure gradient region in the low ρ* case, the calculated edge bootstrap current profile in the equilibrium reconstruction was narrower than at higher ρ*. Combining these in the peeling-ballooning stability calculation produced a higher toroidal mode number for the most unstable mode and, consequently, a prediction of a narrower ELM onset region at low ρ*. For these similarity experiments, the discharges at reduced ρ* (by increased B_T) also were at higher density, $n^{ped} \sim B_T^{4/3}$. Therefore, the narrowing of the steep gradient of the pressure was due in part to reduced neutral penetration at high density in this ρ* scan.

C. ELM DYNAMICS IN THE PEDESTAL AND MIDPLANE SOL

Midplane and SOL ELM dynamics measurements show large, rapid variations of the SOL parameters and suggest a filamentary structure of the perturbation with fast radial propagation in later phases, and parallel propagation of the ELM pulse at speeds approaching the sound speed of pedestal ions. Previous measurements confirmed the expected outer midplane dominated peeling-ballooning spatial structure at ELM onset [43,44]. A reduction of n_e^{ped} was seen at all densities during an ELM and T_e^{ped} was also reduced at low n_e^{ped} ("conductive" ELMs) but no change to T_e^{ped} was seen during ELMs at high density ("convective" ELMs) [44]. Scanning reflectometer data show that the particles lost from the pedestal during an ELM appear far out in the SOL at the midplane [45]. This result was independent of the pre-ELM density. In the far outer SOL where n_e^{SOL} increases substantially, no increase in T_e^{SOL} was observed, implying rapid parallel conduction of the ELM energy in the SOL. Fast CER measurements showed similar loss of impurities from the pedestal, a drop in pedestal toroidal and poloidal rotation, and the elimination of the pedestal electric field well by the ELM crash [46]. Scanning probe data near the separatrix showed large, rapid variations of both n_e^{SOL} and T_e^{SOL} during ELMs suggesting a filamentary structure of the perturbation [47]. This interpretation was supported by recent data from an ultra-fast radial interferometer chord (Fig.6) At the time of the ELM crash, the line integrated density at the midplane showed a burst of high frequency oscillations for ≈100 μs, consistent with the duration of the ELM perturbation on the fast magnetics signals. Beam Emission Spectroscopy (BES) data (Fig.7) [47] also showed the development of a poloidally localized density "finger" that breaks away from the pedestal at the ELM crash. Finally, CIII (465nm) visible emission data from a tangentially viewing fast-gated camera [48] at the midplane (Fig.8), showed multiple filaments extended along the SOL flux surfaces. Toroidal mode number of these filaments, inferred from the CIII images, is $15 < n < 20$. ELITE calculations (Figs.8(c),(e)), for the case in Fig.8(f), show a toroidal mode structure of the most unstable modes in the range

$14 < n < 24$ at $q \sim 4$. CER measurements indicated that the ELM density perturbation structure may be toroidally rotating in the SOL [47,49]. The radial velocity of the density perturbation, inferred from both the probe and reflectometer data, was ~700m/s near the separatrix. The radial velocity decreases with radius in the SOL. Parallel velocity of the density perturbation, inferred from the relative timing of the D_α pulses in the two divertors, approached the sound speed of ions at the pedestal temperature [50].

Poloidal and toroidal narrowing of the density perturbation into filaments (Figs.(9) and (10)) were seen in nonlinear ELM simulations [51] with the BOUT code [52]. BOUT solves the 2- fluid Braginski equations in field line following coordinates. These simulations used conditions of a high density DIII–D discharge with small, convective ELMs. ELITE indicated that the starting conditions used in these simulations were beyond the linear instability threshold. The projection of the density perturbation, from all of the flux tubes in the simulation, onto a poloidal plane (Fig.9(a)) in the linear phase of the mode growth shows the outer midplane dominated structure of the perturbation expected from peeling-ballooning theory. At this stage the perturbation has a toroidal mode number, $n \sim 20$ (4 lobes in 1/5 of the torus in Fig.10(a)) and has a linear growth rate normalized to the Alfven frequency of $\gamma/\omega_A \sim 0.15$. When the growth becomes nonlinear, the density perturbation becomes more poloidally and toroidally localized (Fig.10(b)). At the ELM crash, the perturbation bursts into the SOL and breaks into filaments (positive and negative perturbation regions poloidally in Fig.9(b) and local finger into the SOL in the midplane cut in Fig.10(c)). This is qualitatively consistent with nonlinear ballooning theory [53]. The simulation shows a substantial drop in the pedestal density and an increase in the far SOL density at the crash, consistent with measurements.

4. SUMMARY AND CONCLUSIONS

Progress has been made toward a quantitative physics understanding that will increase confidence in our ability to predict two critical aspects of future high-power tokamak operation, namely the width of the density pedestal and the pedestal pressure gradient at Type-I ELM onset. Some progress has also been made toward understanding the complex coupling of transport and stability mechanisms that set the temperature pedestal height and width. Given knowledge of n_e^{ped}, Δ_n predicted from a neutral penetration model agrees with present measurements in several experiments. This suggests that neutral penetration physics is playing an important role in determining the density pedestal width, although particle transport in the pedestal must also be understood before predictions of the density pedestal can be made for future devices. The pedestal Δ_T appears to be dominated by plasma physics transport mechanisms not neutral penetration physics. The results suggest that it may be possible to independently control Δ_n, by controlling fueling of the pedestal, either by controlling neutral sources from gas injection as in present devices or perhaps by optimizing particle deposition profiles from fueling systems (*e*.g. pellets, compact toroid injection, etc.) in future devices. Independent control of the edge density profile at fixed temperature profile could allow optimization of the edge bootstrap current to minimize ELM energy loss for a given core confinement. Linear peeling-ballooning stability calculations, using a model of the edge bootstrap current constrained

by j^{edge} measurements, predict instability of intermediate-*n* peeling-ballooning modes for the measured pedestal pressure at ELM onset. They also predict that lower edge current might increase the toroidal mode number of the most unstable mode leading to smaller ELMs. The reduction of measured ELM energy loss with decreasing ρ* in the similarity experiments was consistent with increased *n*-number of the most unstable mode leading to narrower ELM affected region in the edge. This suggests that tolerable sized ELMs may be possible in future devices at low ρ* and high density. In addition, the lack of ρ* dependence of Δ_T/a also suggests favorable confinement in future devices with small ρ*. Finally, recent fast measurements of ELM dynamics in the midplane pedestal and SOL show evidence for a filamentary structure of the perturbation at the nonlinear ELM crash. Initial non-linear fluid simulations show a poloidally and toroidally localized density perturbation at the crash leading to a filamentary structure in the SOL, in qualitative agreement with the data.

ACKNOWLEDGEMENTS

This work was performed under the auspices of the U.S. Department of Energy by University of California Lawrence Livermore National Laboratory under Contract Nos. W-7405-ENG-48, DE-FC02-04ER54698, and Grant Nos. DE-FG02-04ER54758, DE-FG03-96ER54373, and DEFG03-01ER54615.

REFERENCES

[1]. ITER Physics Expert Groups, *ITER Physics Basis* 1999, Nucl. Fusion, **39** (1999) 2175.
[2]. T.H. Osborne, *et al.*, Plasma Phys. and Control. Fusion **42** (2000) 1.
[3]. G. Federici, *et al.*, J. Nucl. Mater. **313–316** (2003) 11.
[4]. A. Kirk, *et al.*, Plasma Phys and Control. Fusion **46** (2004) A187
[5]. J. Hughes, *et al.*, Phys. Plasmas **9** (2002) 3019.
[6]. I. Nunes *et al.*, Proc. 31st EPS. Conf. on Plasma Physics and Controlled Fusion, London, UK, 2004 (ECA) P4-137.
[7]. L.D. Horton *et al.*, "Characterization of the H–mode Barrier in ASDEX-Upgrade," Proc. 20th IAEA Fusion Energy Conf., Villamoura, Portugal, EX/P3-4, to be submitted to Nucl. Fusion.
[8]. A. Kallenbach,"*et al.*, Plasma Phys and Control. Fusion **46** (2004) 431.
[9]. R.J. Groebner, *et al.*, Plasma Phys and Control. Fusion **40** (1998) 673
[10]. D. Mossessian, *et al.*, Phys Plasmas, **10** (2003) 689.
[11]. G. Saibene, *et al.*, Plasma Phys. and Control. Fusion **46** (2004) A195.
[12]. A. Hermann, *et al.*, J. Nucl. Mater. **313–316** (2003) 759.
[13]. J. Neuhauser *et al.*, Plasma Phys. and Control. Fusion **44** (2002) 855.
[14]. I. Nunes *et al.*, Proc. 30th EPS. Conf. on Plasma Physics and Controlled Fusion, St. Petersburg, Russia, 2003 (ECA) P1-157.
[15]. P. Ghendrih *et al.*, J. Nucl. Mater. **313–316** (2003) 914.

[16]. B. Goncalves *et al.*, Plasma Phys. and Control. Fusion **45** (2003) 1627.
[17]. A.V. Chankin *et al.*, Nucl. Fusion **43** (2002) 733.
[18]. A.V. Chankin *et al.*, J. Nucl. Mater. **313–316** (2003) 828.
[19]. G. Counsell *et al.*, Plasma Phys. and Control. Fusion **44 (**2002**)** 827.
[20]. G. Counsell *et al.*, J. Nucl. Mater. **313–316** (2003) 804.
[21]. R. Pitts *et al.*, Nucl. Fusion **43** (2003) 1145.
[22]. A. Loarte, *et al.*, Phys. Plasmas **11** (2004) 2668.
[23]. M. Kempenaars, *et al.*, Proc. 30th EPS Conf. on Control. Fusion and Plasma Phys., St. Petersburg, Russia, ECA Vol. 27A (2003) P1.92.
[24]. D.M. Thomas, *et al.*, Phys. Rev. Lett. **93** (2004) 65003.
[25]. R.J. Colchin, *et al.*, Rev. Sci. Instrum. **74** (2003) 2068.
[26]. J.A. Boedo, *et al.*, Rev. Sci. Instrum. **69** (1998) 2663; J.A. Boedo, *et al.*, Rev. Sci. Instrum. **70** (1999) 2997.
[27]. L. Zeng, *et al.*, Rev. Sci. Instrum. **74** (2003) 1530; G. Wang, *et al.*, Rev. Sci. Instrum. **74** (2003) 1525.
[28]. G.R. McKee, *et al.*, Rev. Sci. Instrum. **70** (1999) 2179; McKee, G.R., *et al.*, Rev. Sci. Instrum. **74** (2003) 2014.
[29]. M.A. Vanzeeland, and T.N. Carlstrom, accepted for publication in Rev. Sci. Instrum. **75** (2004); M.A. Vanzeeland, private communication.
[30]. F. Wagner, and K. Lackner, Phys. Plasmas-Wall Interactions in Controlled Fusion, NATO ASI Series B, Physics (1986) Vol. 131, p. 931.
[31]. W. Engelhardt and W.J. Feneberg, J. Nucl. Mater. **76–77** (1978) 518.
[32]. M.A. Mahdavi, *et al.*, Phys. Plasmas **10** (2003) 3988, and Mahdavi, M.A., *et al.*, Nucl. Fusion **42** (2002) 52.
[33]. F.L. Hinton, and Staebler, G.M., Phys. Fluids B **5** (1993) 1281.
[34]. D.A. Mossessian, P.B. Snyder, A. Hubbard, *et al.*, Phys. Plasmas **10** (2003) 1720; D.A. Mossessian, Proc. 30th EPS. Conf. on Plasma Physics and Controlled Fusion, St. Petersburg, Russia, 2003 (ECA) Vol. 27A, P3.182.
[35]. D.M. Thomas, *et al.*, Proc. 31st EPS. Conf. on Plasma Physics and Controlled Fusion, London, UK, 2004 (ECA) Vol. 28G, P2.177.
[36]. D.M. Thomas, *et al.*, Rev Sci. Instrum. **74** (2003) 1541; D.M. Thomas, *et al.*, Rev. Sci. Instrum. **75** (2004) 4109.
[37]. D.M. Thomas, *et al.*, Bull. Am. Phys. Soc. **49** (2004) 209 to be submitted to Phys. Plasmas.
[38]. W.A. Houlberg, *et al.*, Phys. Plasmas **4** (1997) 3230.
[39]. T.A. Casper, *et al.*, Proc. 30th EPS. Conf. on Plasma Physics and Controlled Fusion, St. Petersburg, Russia, 2003 (ECA) P3.207.
[40]. P.B. Snyder, *et al.*, Phys. Plasmas **9** (2002) 2037; Snyder, P.B., *et al.*, Nucl. Fusion **44** (2004) 320.
[41]. H.R. Wilson, *et al.*, Phys. Plasmas **9** (2002) 1277.
[42]. M.A. Mahdavi, *et al.*, J. Nucl. Mater. **162–164** (1988) 245.

[43]. T.W. Petrie, *et al*., Nucl. Fusion **43** (2003) 910.

[44]. A.W. Leonard, *et al.*, J. Nucl. Mater. **313–316** (2003) 768; A.W. Leonard, *et al.*, Phys. Plasmas **10** (2003) 1765.

[45]. L. Zeng, *et al.*, Plasma Phys. Control. Fusion **46** (2004) A121; Zeng, L., *et al.*, "SOL and pedestal density evolution in DIII–D H–mode," accepted for publication in J. Nucl. Mater. (2004).

[46]. M.R. Wade, *et al.*, "Time resolved measurement of the impurity, ion, and electron dynamics during an ELM cycle," Phys. Rev. Lett., submitted (2004).

[47]. J.A. Boedo, *et al*., "ELM dynamics and transport in the SOL of the DIII–D tokamak," submitted for publication in Phys. Plasmas (2004).

[48]. M. Groth, *et al.*, Rev. Sci. Instrum. **74** (2003) 2064.

[49]. J.A. Boedo, *et al*., "ELM-induced plasma transport in the DIII–D SOL," Proc. 31st EPS. Conf. on Plasma Physics and Controlled Fusion, London, UK, 2004.

[50]. M.E. Fenstermacher, *et al.*, Plasma Phys. Control. Fusion **45** (2003) 1597; M.E. Fenstermacher, *et al*., accepted for publication in J. Nucl. Mater. (2004).

[51]. P.B. Snyder, H.R. Wilson, X.Q. Xu., and A.J. Webster, "Progress in the peelingballooning model of ELMs: Numerical studies of 3D nonlinear dynamics," accepted for publication in Phys. Plasmas (2004).

[52]. X.Q. XU, *et al.*, Nucl. Fusion **40** (2000) 731.

[53]. H.R. Wilson, and S.C. Cowley, Phys. Rev. Lett. **92** (2004) 17500

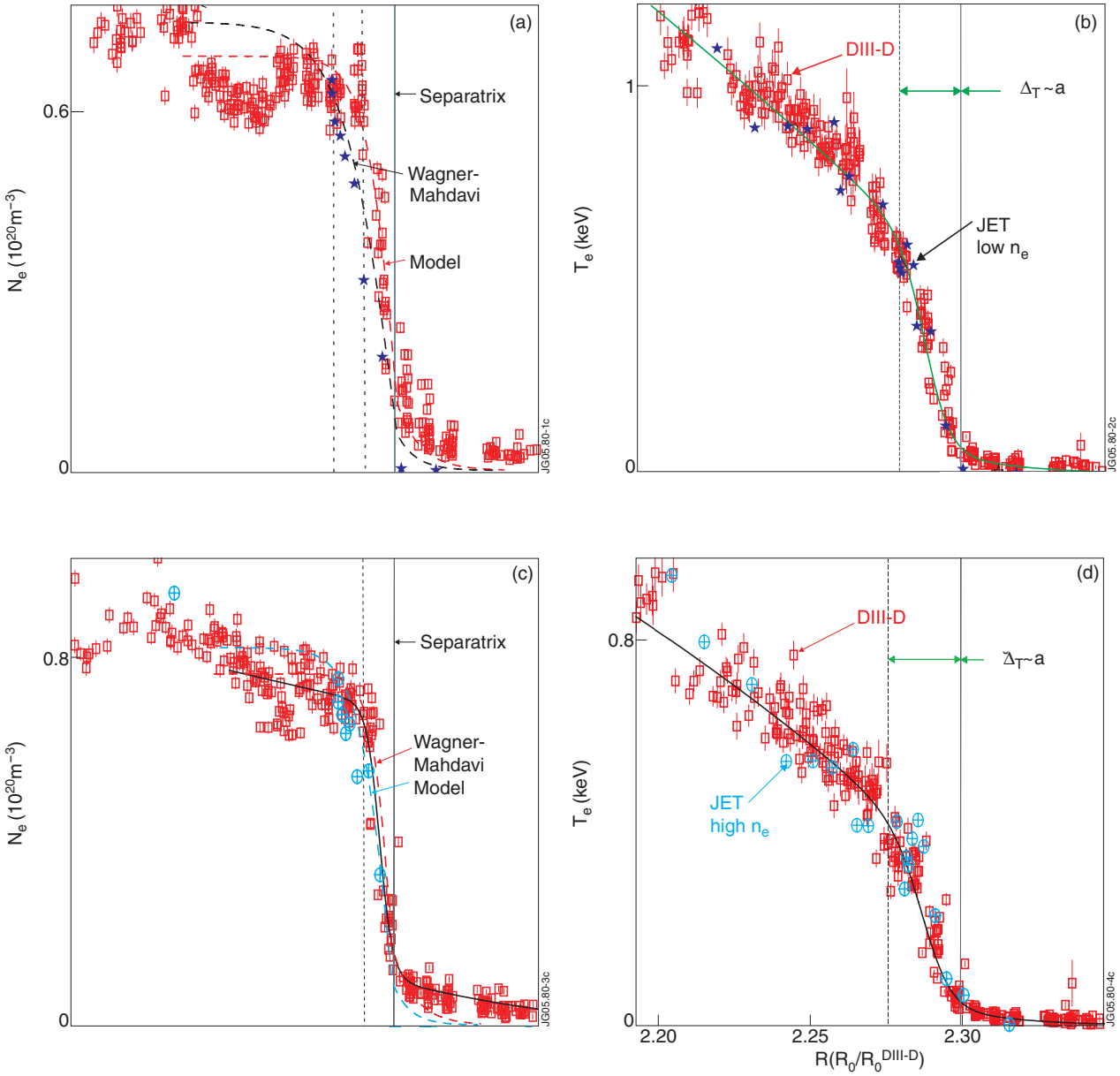

Figure 1: Comparison of density (a,c) and temperature (b,d) pedestal profiles in DIII–D and JET for low (a,b) and high (c,d) density H–mode operation in the similarity experiments. Predictions of the profiles from a neutral penetration model are shown as dashed curves in (a,c) for both DIII–D and JET. Vertical lines mark the separatrix (solid), and the top of the pedestals for DIII–D (dashed) and JET (long dashed). Temperature profile width scales with minor radius (b,d). DIII–D data is from 20% to 40% of the ELM cycle. B_T (DIII–D) = 2.1T, B_T (JET) = 1.2T. Density scaled to DIII–D as–$n_e \propto \alpha^{-2}$ *temperature scaled to DIII–D as* $T_e \propto \alpha^{-1/2} A^{5/4}$.

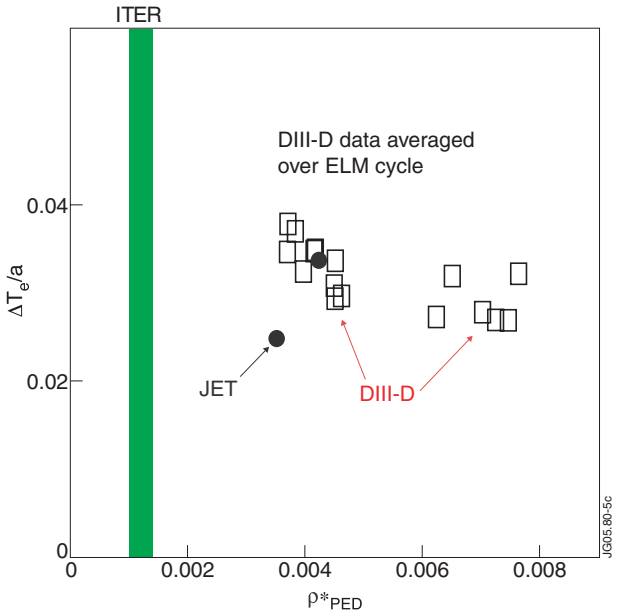

Figure 2: Normalized temperature pedestal (transport barrier) width, Δ_T/a, as a function of ρ at the top of the pedestal from DIII–D/JET similarity experiments. Data does not show a strong dependence with ρ*.*

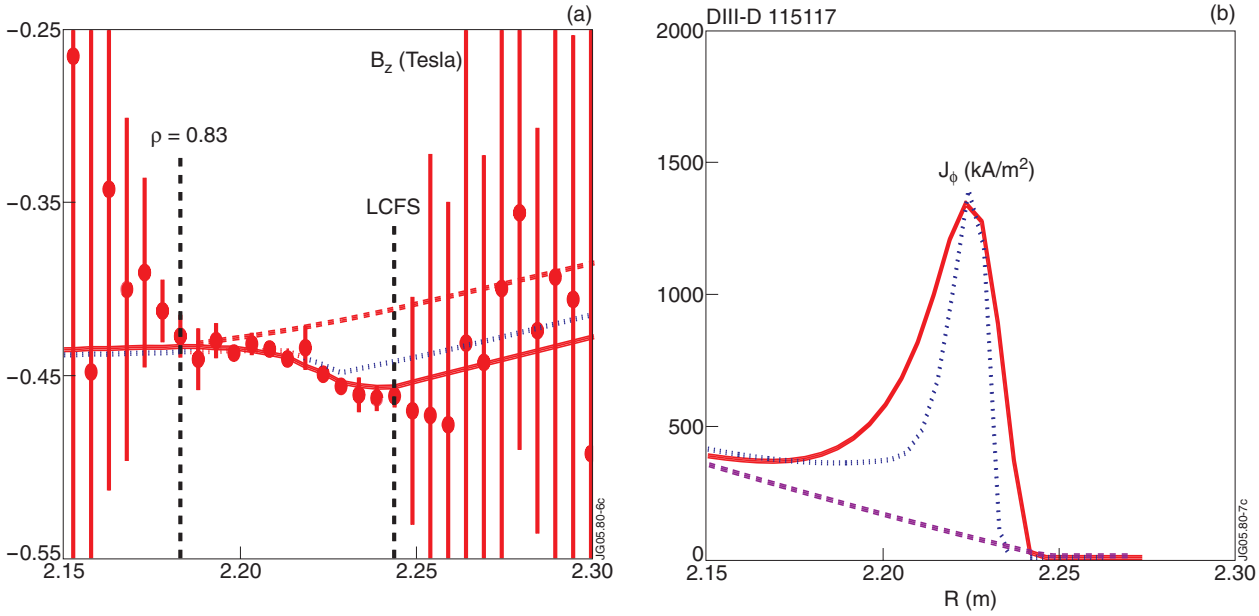

Figure 3: Li-beam polarimetry measurements of the pedestal poloidal field profile (a), and the inferred edge current density profile (b), for plasma conditions just before ELM onset. The measured profiles (solid) are compared with calculated values using an equilibrium reconstruction code constrained by the NCLASS bootstrap current model (dotted), and with measured L–mode phase profiles (dashed). A significant increase in the edge current is seen between L–mode and the profile in H mode just before an ELM. The measured current density peak of 1.35 MA/m^2 agrees well with the calculated value.

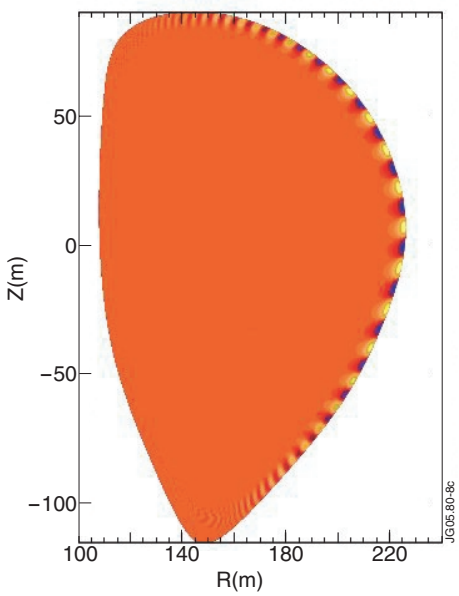

Figure 4: The ELITE prediction of the poloidal mode structure (density perturbation) for the most unstable mode in a kinetic equilibrium reconstructed using the edge current from Fig.3 as a constraint. Positive perturbation is white, negative perturbation is black, no perturbation is gray.

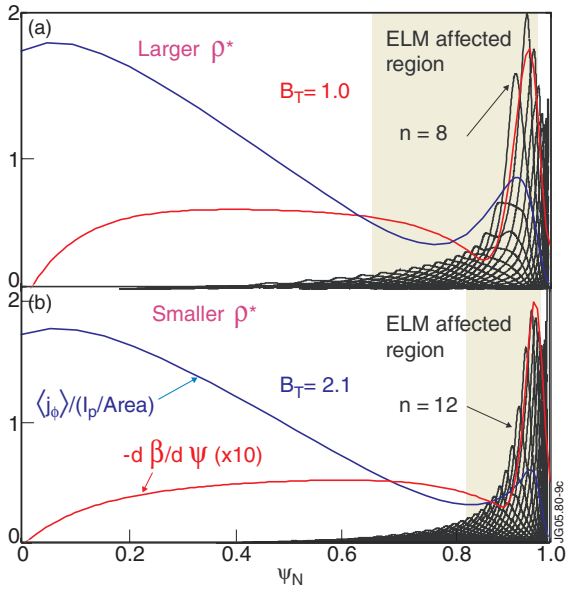

Figure 5: Measured pressure gradient profile (–dβ/dψ), calculated normalized current profile [⟨j$_\phi$⟩/(Ip/Area)] and most unstable peeling-ballooning mode eigen functions for large (a) and small (b) ρ from the DIII–D/JET similarity experiments. The ELM affected area is reduced for smaller ρ*.*

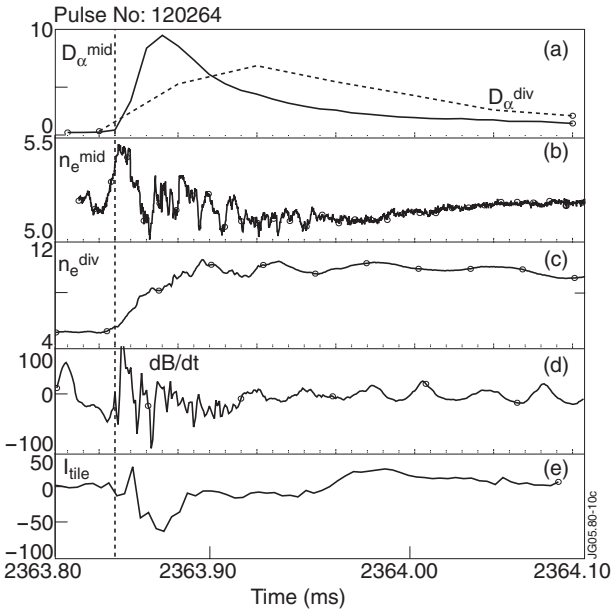

Figure 6: Fast measurements of midplane dynamics during an ELM crash; (a) midplane and divertor D_α emission (a.u.), (b) line averaged midplane density from radial interferometer chord (10^{19} m^{-3}), (c) line averaged divertor density from a vertical interferometer chord (10^{19} m^{-3}), (d) dB/dt (T/s), (e) current integrated on divertor tile (A). ELM crash onset marked by vertical dotted line. Two percent of the data points are marked with circles to indicate the temporal resolution.

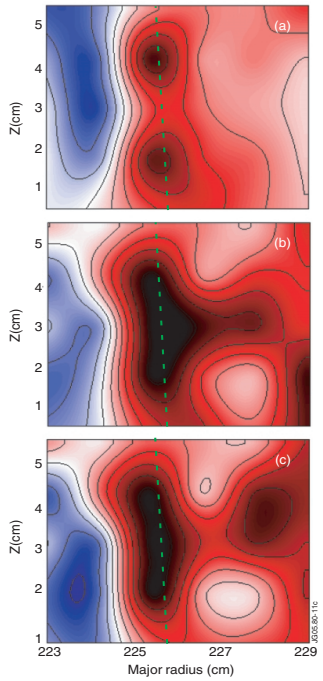

Figure 7: Deviation of density (red-positive, blue-negative) from average (white) near the poloidal midplane (a) between ELMs, and (b,c) during ELM build-up and crash. The ELM perturbation is highly localized poloidally and propagates radially into the SOL. Separatrix at 225.6cm.

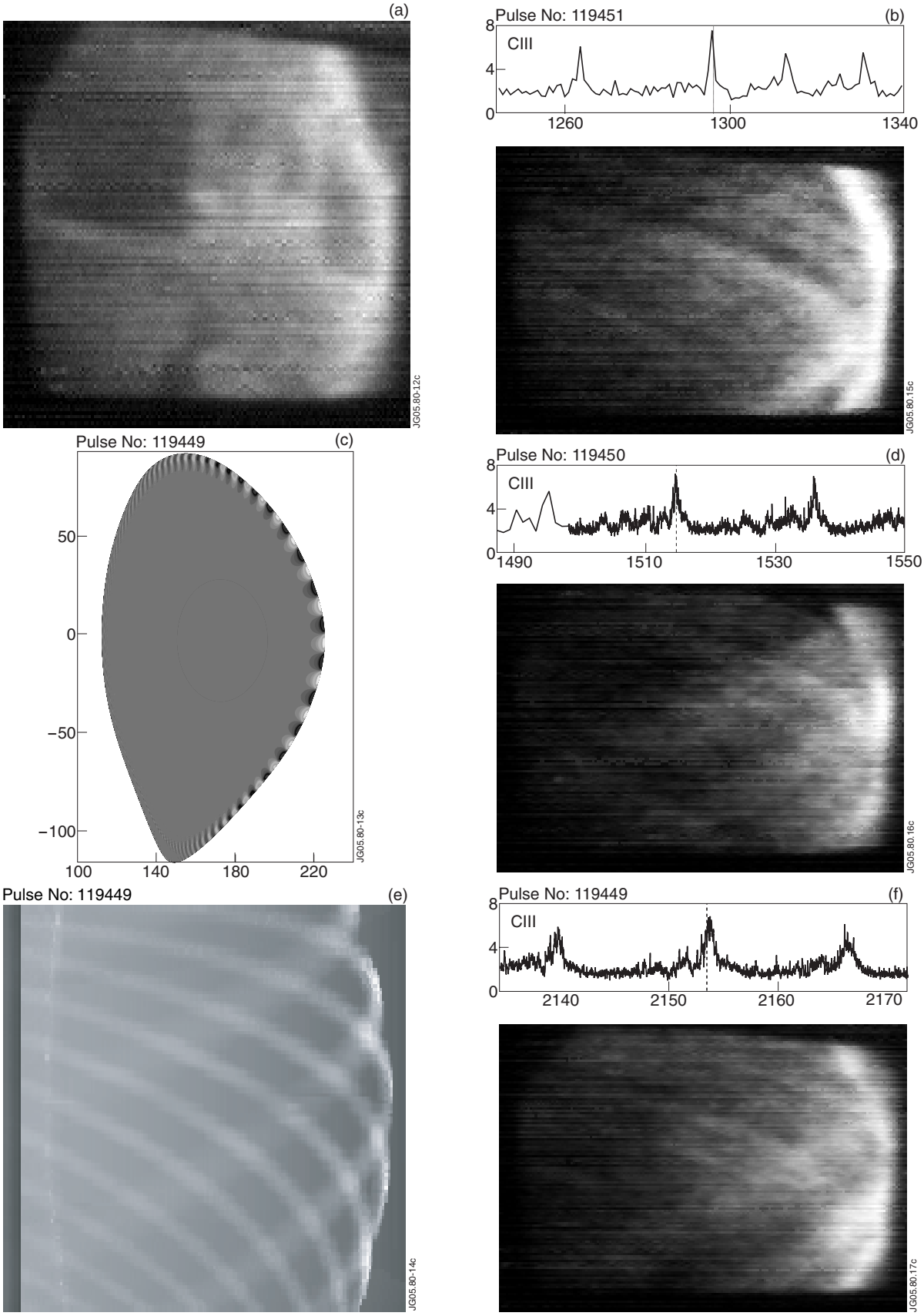

Figure 8: CIII (465nm) images with 10μs exposure during ELM crashes and ELITE simulation results. (a) Camera view of vacuum vessel in reflected light, (b,d,f) images of CIII emission during different ELM crashes, (c) 2D profile of instability mode from ELITE for case shown in (f), (e) camera view of 3D mode structure from ELITE for case (f).

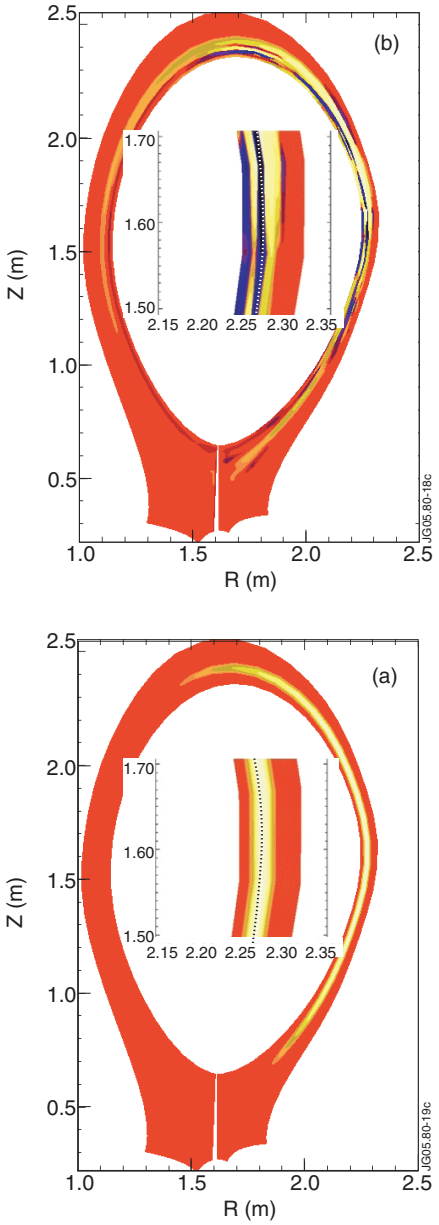

Figure 9: Density perturbation from multiple flux tubes in the pedestal and SOL projected onto a poloidal plane from (a) linear growth phase and (b) nonlinear crash phase of BOUT nonlinear ELM simulation. Inset shows expansion of region near the outer midplane. Unperturbed density is in red, positive perturbation in yellow, and negative perturbation in blue.

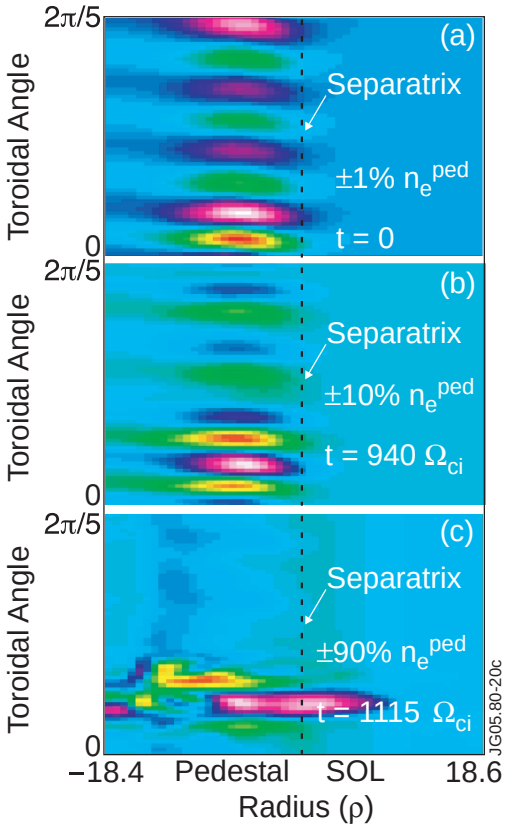

Figure 10: Density contours versus toroidal angle and radius from BOUT nonlinear ELM simulation showing (a) instability mode structure during linear growth phase, (b,c) nonlinear growth of toroidally localized density perturbation and radial propagation at ELM crash. Data shown is a plan view of 1/5 of the torus at the outer equatorial midplane. Unperturbed density is in light blue, positive perturbation in purple-white, and negative perturbation in yellow-red. Color scale range indicated: ±1% n_e^{ped} in (a), ±10% n_e^{ped} in (b), ±90% n_e^{ped} in (c).